



## Engineering Computations

Shape optimization of annular S-ducts by CFD and high order polynomial response surfaces

Eero Immonen,

### Article information:

To cite this document:

Eero Immonen, "Shape optimization of annular S-ducts by CFD and high order polynomial response surfaces", Engineering Computations, <https://doi.org/10.1108/EC-08-2017-0327>

Permanent link to this document:

<https://doi.org/10.1108/EC-08-2017-0327>

Downloaded on: 25 March 2018, At: 01:16 (PT)

References: this document contains references to 0 other documents.

To copy this document: [permissions@emeraldinsight.com](mailto:permissions@emeraldinsight.com)

The fulltext of this document has been downloaded 5 times since 2018\*



Access to this document was granted through an Emerald subscription provided by emerald-srm:123756 []

### For Authors

If you would like to write for this, or any other Emerald publication, then please use our Emerald for Authors service information about how to choose which publication to write for and submission guidelines are available for all. Please visit [www.emeraldinsight.com/authors](http://www.emeraldinsight.com/authors) for more information.

### About Emerald [www.emeraldinsight.com](http://www.emeraldinsight.com)

Emerald is a global publisher linking research and practice to the benefit of society. The company manages a portfolio of more than 290 journals and over 2,350 books and book series volumes, as well as providing an extensive range of online products and additional customer resources and services.

Emerald is both COUNTER 4 and TRANSFER compliant. The organization is a partner of the Committee on Publication Ethics (COPE) and also works with Portico and the LOCKSS initiative for digital archive preservation.

\*Related content and download information correct at time of download.

# Shape optimization of annular S-ducts by CFD and high order polynomial response surfaces

---

## Abstract

**Purpose.** This article aims to design an optimal shape for an annular S-duct, considering both energy losses and exit flow uniformity, starting from a given baseline design. Moreover, this article seeks to identify the design factors that affect the optimal annular S-duct designs.

**Methodology.** We carry out CFD-based shape optimization relative to 5 distinct numerical objectives, in order to understand their interrelations in optimal designs. Starting from a given baseline S-duct design, we apply control node induced shape deformations and high order polynomial response surfaces for modeling the functional relationships between the shape variables and the numerical objectives. A statistical correlation analysis is carried out across the optimal designs.

**Findings.** We show by single-objective optimization that the two typical goals in S-duct design, energy loss minimization and exit flow uniformity, are mutually contradictory. We present a multi-objective solution for an optimal shape, reducing the total pressure loss by 15.6% and the normalized absolute radial exit velocity by 34.2% relative to a baseline design. For each of the 5 numerical objectives, the best optimization results are obtained by using high-order polynomial models.

**Limitations.** The methodology is applicable to axisymmetric 2D geometry models.

**Originality.** This article applies a recently introduced shape optimization methodology to annular S-ducts, and, it is, to the author's knowledge, the first paper to point out that the two widely studied design objectives for annular S-ducts are contradictory. This article also addresses the value of using high-order polynomial response surface models in CFD-based shape optimization.

**Keywords:** CFD, S-duct, response surface, endwall contouring, shape optimization,

## 1. Introduction

Annular ducts of the *S-shape* are important components in various mechanical devices. For example, in a modern aircraft gas turbine engine, an annular S-shaped transition duct connects its low- and high-pressure systems by transmitting flow from a high radius region to a low radius region. In engine design, there is a constant need to reduce equipment weight and improve fuel efficiency. Transition ducts that are increasingly more *aggressive*, i.e. are shorter in axial length and have a larger radial offset, have been identified as a key element in the design of such high-performance engines. The optimal design of efficient S-shaped ducts necessitates an understanding, and control, of the complex flow patterns within the ducts. The more aggressive the duct shape is, the more prone flow within it is to separate and display a non-uniform outlet profile that may, for instance, adversely affect the surge performance of a downstream compressor.

Over the years, several researchers have carried out *experimental* investigation of flow in S-ducts [1, 2, 3], and observed that it is strongly influenced by the duct's streamwise curvature. Bailey et al. [3] concluded that this curvature also affects the generation and suppression of turbulence. On the other hand, Britchford et al. [2] observed that a compressor stage at the inlet reduces the tendency of flow to separate on the inner (hub) wall. Finally, Dueñas et al. [4] carried out an investigation on the development of boundary layers and losses within S-shaped ducts, by varying their axial length. While these experimental studies have significantly enhanced the understanding of flows in annular S-ducts, the time-consuming and expensive experimental approach is not ideal for modern engineering shape optimization and design.

The superior flexibility and cost-efficiency in evaluating new design candidates relative to physical prototypes, the abundance of off-the-shelf solvers, and the arrays of validation studies for well-known benchmark reference cases, have gradually made the use of computational fluid dynamics (CFD) standard practice in engineering design. Indeed, CFD methods have recently been successfully applied in shape optimization of airfoils [5], aircraft compo-

nents [6], ship hulls [7], turbine blades [8, 9], cars [10], industrial processes [11] and even a cardiovascular surgery [12] and the venous system [13], among others. The methods of CFD-based shape optimization can be roughly divided into two categories: *Parametric* and *non-parametric*. In the former approach, the shape is described by a small set of parameters and optimization is carried out by varying them [14]. Usually this is specifically done via a parametric input-output function — a so-called surrogate model, response surface model (RSM), or metamodel — for which the performance metrics are first regressed on the shape variables; optimization is then an elementary step on the surrogate function [14, 15, 16, 17]. On the other hand, in non-parametric shape optimization, a baseline shape is deformed, usually guided by a simple gradient-based optimization routine, towards a solution which aims to improve the objective function [18]. Recently, Immonen [5] introduced a CFD-based shape optimization method halfway between these two categories by considering parametric *deformations* of a nominal shape.

Ghisu et al. [19] used a modified gradient-based approach for optimizing axial compressor intermediate duct wall shapes by using CFD. By varying effectively 3 of the total 11 duct geometry variables, they were able to reduce the total pressure loss in the S-duct by 12.5%. Wallin and Eriksson [20] utilized RSMs and design of experiments (DOE) for CFD-based optimization of compressor transition ducts. They reported a reduction of 24% in the S-duct's total pressure loss. Lu et al. [21] recently introduced a combinatorial optimization method, based on uniform design and RSM incorporating CFD, for improving S-shaped compressor transition duct design. According to Lu et al. [21], the uniform design principle can reduce the number of candidate designs for RSM identification, relative to the common face-centered composite design method. By using this technique, they were able to reduce the total pressure loss in the duct by 36.9% and obtain more uniform distributions of parameters at the outlet. Naylor et al. [22] investigated CFD-based optimization of non-axisymmetric endwalls in strutted compressor S-ducts by a radial basis function RSM approach. They report a reduction of 16% in the net duct loss as a result of endwall profile optimization. Yurko and Bondarenko [23] provided design guidelines for annular S-ducts with inlet guide vanes, based on CFD design optimization utilizing Bézier curve parameterizations.

The thus far reported scientific research on optimal endwall shaping for annular S-ducts appears to proceed via minimization of energy losses by case-specific methods; flow uniformity at the outlet can then potentially be obtained as a favorable *by-product* (e.g. [21]). Indeed, it seems that the effect of minimizing the total pressure loss on the outlet flow profile uniformity, and other well known performance metrics (see e.g. [24]), have received relatively little attention in the academic literature. In the present article, we carry out shape optimization for annular S-ducts relative to 5 distinct numerical design objectives, each addressing energy losses and flow uniformity in different ways, in order to understand their interrelations in optimal designs. Our shape optimization method is adapted from Immonen [5], and we utilize high order polynomial response surfaces for modeling the functional relationships between the design variables and the output objectives. We demonstrate that the parametric control node deformation method of Immonen [5] can easily accommodate any number of alternative objective functions *simultaneously* (though only 2 were considered in [5]); a statistical correlation analysis across the optimal solutions may then yield new insights into the optimal design of the equipment under consideration. The proposed method is not guaranteed to produce the global optimum shape, but, as demonstrated, the baseline model can be significantly improved.

The presence of the S-shaped bend, which endwall contouring cannot remove, has been shown by many researchers to induce a non-uniform velocity distribution and to result in zones of separation along the wall surfaces [25]. We demonstrate, by the statistical correlation analysis described above, that, in fact, minimization of total pressure loss in an annular S-duct may induce *additional* radial flow and thus *adversely* affect the flow uniformity at the S-section outlet. Although related to a specific geometry model in the present article, to the author's knowledge, this observation has not been documented in the academic literature before. Further, by addressing energy losses and minimum radial flow in a multi-objective optimization, we show that the nominal S-duct shape can be improved relative to both objectives.

For each numerical optimization objective considered herein, we observe that polynomial response surfaces of orders higher than 2 (the default choice in the literature) not only im-

prove the RSM fit, but also produce better optimization results. This observation contrasts the findings of Immonen [5] who did not find material benefit in using polynomial response surface models of degrees higher than 2 for airfoil shape optimization with respect to drag and lift.

This article is organized as follows. In Section 2 we describe the steps of the proposed approach to shape optimization, and introduce the 5 numerical design objectives for annular S-ducts. The proposed optimization process starts from a baseline S-duct model; the one considered in this study is introduced and analysed in detail in Section 3. After validating the baseline model, in Section 4 we optimize its endwall profiles relative to the 5 objectives. The objectives are first treated independently in Subsection 4.1, and then in combination in a multiobjective setting in Subsection 4.2. The conclusions of the present study are finally documented in Section 5.

## 2. Methodology

The proposed shape optimization process is described schematically in Figure 1. The following subsections describe each step of the process in more detail.

### 2.1. Baseline model with CFD validation

In the proposed framework, shape optimization begins from a baseline design which is to be improved relative to a number of chosen performance metrics. Once the baseline CFD simulation model has been created, its performance is validated by known data from measurements and by checking robustness with respect to changes in spatial discretization and submodel selection. This step involves reiteration of the computational mesh until a sufficient compromise is obtained with respect to result accuracy and speed of convergence.

In fluid flow simulations, we confine our attention to turbulent steady state conditions. We use ANSYS Fluent R16.0 with the double precision, SIMPLE pressure-velocity coupling and second order accuracy options for solving the Reynolds-Averaged Navier-Stokes (RANS) equations of turbulent fluid flow motion, and include a turbulence closure model based on recommendations of academic literature. The objective of the turbulence model for the

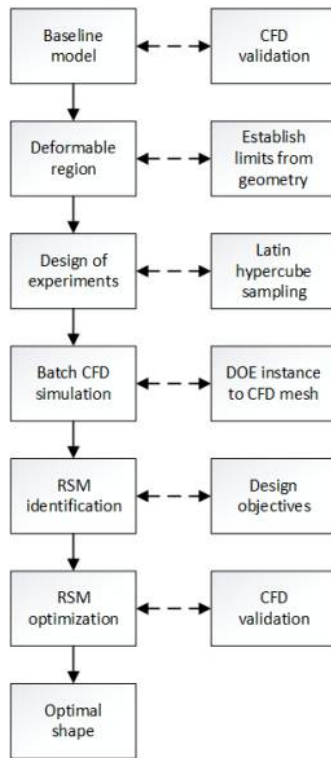


Figure 1: Schematic diagram of the proposed shape optimization process.

RANS equations is to compute the Reynolds stresses. The number of steady state iterations required for flow field convergence is identified from the baseline model and this iteration count held constant across all remaining CFD simulations (with residual-based convergence verification carried out afterwards).

## 2.2. The deformable region and shape deformations

The proposed shape optimization framework relies on carefully constructed deformations of the walls of the baseline duct model. As the objective of this article is to specifically improve the S-shaped section, all deformations are confined to the S-section between the two dashes in Figure 3a, which is also shown in Figure 2 (dashed lines).

For shape deformations, we adapt the *control node* approach introduced by Immonen [5] as follows. First, two equidistant control nodes are placed symmetrically on both endwalls of the S-section. These four control nodes are then allowed to be moved in the radial direction, resulting in 4 shape parameters (i.e. the radial control node displacements). Subsequently,

the radial displacement profiles for *all other end wall points* are obtained from these four parameter values — and the assumption of zero radial displacements beyond the S-section end points — by one-dimensional piecewise cubic Hermite interpolation. Finally, the actual deformed hub and casing wall shapes are obtained by applying the interpolated displacement profiles while moving all boundary nodes in the radial direction, as illustrated in Figure 2. We emphasize that the endwall profiles thus obtained are not instances of a particular parametric function family; indeed, in the method of Immonen [5], it is *deformations*, not shapes, that are parametric. Consequently, the variation among the deformed shape candidates is large, which potentially makes the RSM identification process more robust and the subsequent optimization process less susceptible to only reaching a local optimum.

For the baseline geometry model considered in the present article, a maximum limit for the displacement of the control nodes is set at  $\pm 2$  mm relative to initial (zero-displacement) position, based on experimentation. Similar to Donghai et al. [26], in an attempt to only produce smooth deformed shapes — to maintain a reasonable continuity of profile shape derivatives near the S-section end points — zero nodal displacements are additionally required in the last 4% of the S-section nodes near the two end points. The displacement bounds for the remaining points are obtained by piecewise cubic Hermite interpolation of the extreme values (see Figure 2).

### 2.3. Design of experiments

Response surface identification typically requires a least-squares fit on a representative input-output data set of the underlying relation [5]. In CFD-based shape optimization, such data set is obtained via CFD simulations with carefully constructed shape candidates providing “experiments” that associate the input variables (the shape geometry) to the output variables (the performance objectives).

A common approach for designing the set of experiments is through *space filling designs* that aim at covering as much of the input variable space as possible and as evenly as possible. One widely studied space filling design, also utilized in the present work, is the Latin Hypercube Sampling (LHS) method proposed by McKay et al. [27]. It has many well



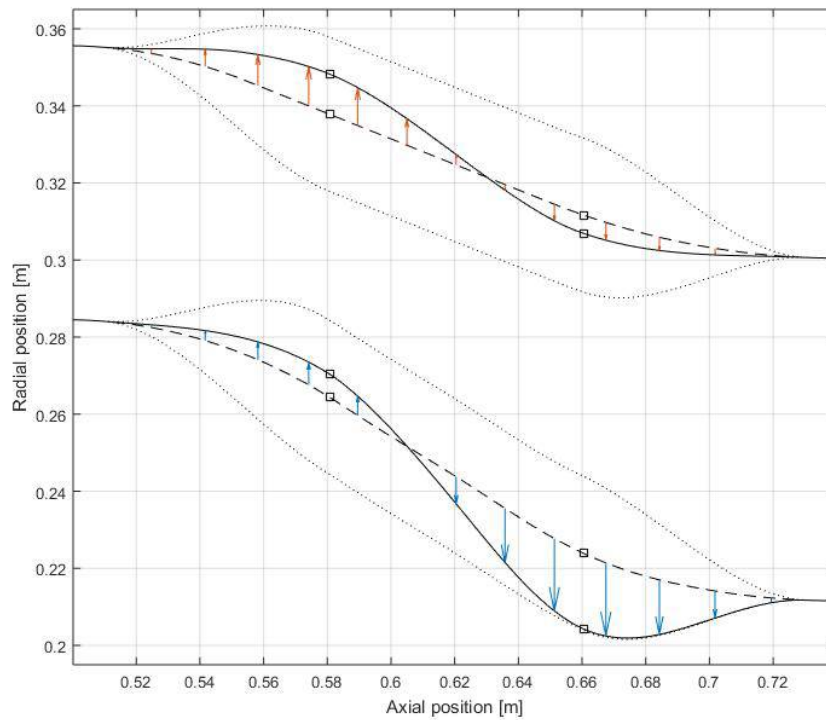


Figure 2: The principle of nodal displacements induced by control nodes [5]. The dashed lines display the baseline geometry model, the squares display the control node locations, and the solid lines display one possible deformed duct profile. Nodal displacements are illustrated by arrows. The dotted lines display the bounds for the deformations.

known merits: The number of design points can be freely chosen, the designs are orthogonal, and the design points are independent of the response surface model to be identified.

In the present work, each row in the DOE table, created by the LHS method, specifies the four displacement values of the control nodes. Since the result of piecewise cubic Hermite interpolation is unique, each such DOE table row also uniquely defines a shape candidate. Consequently, this step yields the input data for RSM identification. The following result from Immonen [5] describes the minimum DOE table size for multivariate polynomial RSM identification.

**Theorem 1.** *Let  $p$  be a  $n$ -variate polynomial of degree  $k$  and consider the set of its  $\rho$  known values:  $V = \{(\mathbf{x}_i, p(\mathbf{x}_i)) \in \mathbb{R}^{n \times 1} \mid 1 \leq i \leq \rho, \mathbf{x}_i \neq \mathbf{x}_j \text{ for all } i \neq j\}$ . If  $V$  uniquely determines*

$p$ , then  $\rho \geq \binom{k+n}{n}$ .

#### 2.4. Batch CFD simulation of the shape candidates

In order to provide the required output data for RSM identification, each deformed S-duct model arising from the DOE set is simulated using the initial and boundary conditions of the baseline model, in a batch process. In order to avoid numerical errors, the mesh structure, especially the boundary layer resolution, of the deformed shape candidates is to be kept equivalent to that in the baseline model. In the present work, this is achieved by using a custom MATLAB-based meshing routine, developed by the author, that creates a structured mesh using a fixed number of axial and radial nodes, and a given boundary layer cell height growth factor (see Figure 3b). Here, the size and growth parameters for the deformed meshes are those identified for the baseline model. This ensures that the change in cell aspect ratios in the cross direction remains constant across the batch. Further, the iteration count in each CFD simulation in the batch set is the same as in the baseline model.

#### 2.5. Design objectives for annular S-shaped ducts

Design optimization of annular S-shaped ducts generally aims at minimizing energy losses and constructing a uniform flow at the exit section of the duct. In this subsection, we define five numerical quantities in Equations (1), (3), (4), (5) and (6), related to these two generic design criteria, that are each reported from the batch CFD simulation results. The RSM (cf. Subsection 2.6) attempts to describe the functional relationship between the shape input parameters and these numerical quantities.

First, let us fix some notation. Let  $P$  and  $p$  denote the total and static pressure in the fluid flow field, respectively. Let  $p_{inlet}$  denote the static pressure, and let  $U_{mean}$  denote the average flow velocity, at the inlet boundary of the S-duct geometry. The velocity magnitude and radial velocity in the flow field are denoted by  $U$  and  $U_r$ , respectively. Let us define  $P_i = \frac{1}{m} \int_{x/L=i} P dm$  and  $p_i = \frac{1}{m} \int_{x/L=i} p dm$  the mass-weighted average of total pressure and static pressure, respectively, at the axial position  $x/L = i$  in the S-duct. Here  $L$  denotes the length of the S-shaped section,  $i = 0$  denotes entry to the S-section, and  $i = 1$  denotes exit from it.

### 2.5.1. Energy losses

The total pressure loss coefficient  $TP$  defined in Equation (1) represents the net energy losses in the S-shaped duct section. This design objective was considered by Lu et al. [21], Yurko et al. [23], Donghai et al. [26], Ghisu and Molinari [19] among others.

$$TP = \frac{P_1 - P_0}{\frac{1}{2}\rho U_{mean}^2} \quad (1)$$

The wall static pressure coefficient  $C_p$  is defined at each point on the hub and casing walls as follows:

$$C_p = \frac{p - p_{inlet}}{\frac{1}{2}\rho U_{mean}^2} \quad (2)$$

Large variations in the pressure coefficient value on the endwalls indicate rapid acceleration and deceleration of the flow, which may then result in flow separation and energy losses. Hence it may be reasonable to design the annular S-duct such that the maximum deviation of  $C_p$  on the hub and casing walls, defined in Equation 3, is minimized.

$$CP = \max \{ \max(C_p|_{hub}) - \min(C_p|_{hub}); \max(C_p|_{casing}) - \min(C_p|_{casing}) \} \quad (3)$$

Similarly, we can consider the standard deviation of static pressure in the flow field:

$$SP = \sigma(p) \quad (4)$$

as a design criterion, with a minimum  $SP$  solution potentially yielding a maximally undistorted flow. Among others, Rose [28] has associated non-uniformity of static pressure to energy losses. Consequently, minimization of  $SP$  and  $CP$  are indirect attempts at minimization of energy losses within the duct — bearing in mind that a nonzero static pressure gradient across the S-section is a pre-requisite for making the flow turn by the effect of centripetal acceleration. Some static pressure variation is thus inevitable in an annular S-duct [29].

### 2.5.2. Flow uniformity

We can quantify non-uniformity of flow at the S-section exit  $x/L = 1$  either by considering standard deviation of normalized velocity magnitude there, as in Equation (5), or by

considering the sum of normalized absolute radial velocity there, as in Equation (6):

$$U_{rel} = \sigma \left( \frac{U|_{x/L=1}}{U_{mean}} \right) \quad (5)$$

$$U_{rad} = \Sigma \left| \frac{U_r|_{x/L=1}}{U_{mean}} \right| \quad (6)$$

These quantities are analogous to the distortion coefficient used for quantifying the non-axisymmetry of the outlet flow from axial diffusers [30]. Moreover, they are analogous to the non-uniformity index and mean standard deviation in axial velocity, both representing deviations from purely axial flow, discussed by Gopaliya et al. [31]. The design of an annular S-duct for a maximally uniform exit flow is then carried out by minimizing  $U_{rel}$  or  $U_{rad}$ .

## 2.6. Multivariate polynomial response surface models

In the present work, shape optimization is carried out on an RSM metamodel  $\hat{y} = f(\mathbf{x})$  identified using the input-output data  $(\mathbf{x}_i, y_i)$  from the DOE specification and the batch CFD simulations. In this article, we consider polynomial response surface models of four variables — the control node displacements — of orders up to five. By Theorem 1, a minimum of 126 DOE points are thus needed for the unique identification of such RSM models. To account for possible convergence issues, numerical errors and to help ensure representativeness of the DOE set, the number of DOE samples is fixed at  $N = 500$  in this article.

RSM identification is carried out by least squares regression. For each objective, defined in Equations (1), (3), (4), (5) and (6), five multivariate polynomial models (of orders 1 – 5 respectively) are identified, resulting in a set of 25 distinct response surface models. The goodness-of-fit of each model is assessed by the usual regression metrics: The mean (MAE) of absolute errors  $\left\{ \frac{|y_n - \hat{y}_n|}{y_n} \right\}_{n=1}^N$ , the standard deviation of absolute errors (MAESTD), and the coefficient of determination ( $R^2$ ) representing the square of the Pearson correlation coefficient between the sampled output  $y$  and the RSM prediction  $\hat{y}$ . We report these metrics by using leave-one-out cross-validation, which generally produces slightly pessimistic results as it estimates the generalisation performance of a model trained on  $N - 1$  samples of data.

## 2.7. Optimization

The performance of the baseline model is improved by RSM optimization. The optimization process results in a  $5 \times 5$  table, with cell  $(i, j)$  describing the performance of the  $i^{th}$  degree polynomial RSM identified and optimized with respect to objective  $j$ . Further, each optimization result is validated by CFD simulations. This information helps assess whether or not the use of high order polynomial models is warranted. In addition, the 25 optimal S-duct profiles thus obtained are each evaluated with respect to all 5 design metrics of Subsection 2.5. This step helps evaluate the relationship between the design objectives, and, in particular, decide if some are mutually contradictory. All validation simulations are carried out with the same settings as in the baseline model.

In this article, for single-objective optimization, we use the standard constrained non-linear programming solver `fmincon` of MATLAB 2015a, with the interior-point algorithm; the only constraints are the maximum displacements of the control nodes. For constrained multi-objective optimization, we employ a controlled elitist genetic algorithm, a variant of NSGA-II [32], implemented in the function `gamultiobj` of MATLAB 2015a. All optimization algorithms are set to progress from the zero initial solution, and the genetic algorithm runs maximum of 2000 generations with population size 1000. Under these settings, the optimization of a polynomial model of 4 variables takes approximately 1 – 5 minutes on a 2.6 GHz laptop computer, depending on the polynomial model degree.

## 3. Baseline simulation model

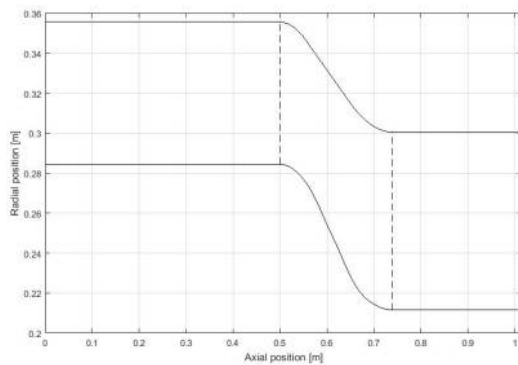
The baseline annular S-duct model we attempt to improve by computational optimization is that of the “clean inlet flow” described by Bailey et al. [3] and Britchford et al. [2, 29] among others.

### 3.1. Geometry and computational mesh

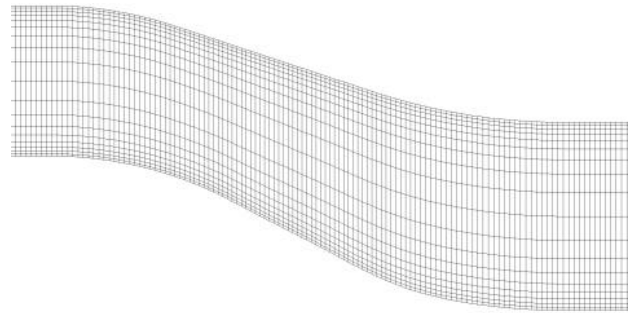
The baseline simulation geometry model is described in Figure 3a. The duct is of constant flow area, i.e. area ratio  $AR = 1$ , with an inlet passage height  $h_{in} = 71.1$  mm, an axial length  $L = 241.74$  mm and an exit-to-inlet mean radius ratio  $MRR = 0.8$ . The radius of

curvature of the mean flow line at inlet is 181.3 mm and at exit 229.65 mm. The S-shaped section, between the dashed lines in Figure 3a, is preceded by an inlet section of 7 hydraulic diameters and a settling outlet section of 3.1 hydraulic diameters. The entry to the S-shaped duct section is labeled  $x/L = 0$  and the exit from the S-shaped section is labeled  $x/L = 1$  following Britchford et al. [2]. Both locations are shown by dashed lines in Figure 3a.

The computational mesh for the baseline geometry model is displayed in Figure 3b. The structured mesh consists of  $412 \times 18 = 7416$  cells, the height of the first cell adjacent to the duct walls is 0.0011 mm across the domain, and the boundary mesh growth rate is 1.3 in the radial direction. This quadrilateral mesh structure, which is subsequently also used in the deformed geometry models, aligns the computational cells with the streamlines and captures the (larger) cross-stream velocity gradient induced by boundary layer flow. The baseline mesh has minimum orthogonal quality 0.879, maximum orthogonal skew 0.120 and maximum aspect ratio 5.464, which metrics indicate that the mesh is of high quality [33].



(a) Axisymmetric geometry



(b) Computational mesh near the S-section

Figure 3: The baseline model adapted from [2, 3] with the S-section between the dashed lines (denoted by  $x/L = 0$  and  $x/L = 1$ ).

### 3.2. Boundary conditions and submodel selection

The velocity inlet (at  $x = 0$  in Figure 3a) is set at  $U_{mean} = 28.3$  m/s. The pressure outlet (at  $x = 1.014$  in Figure 3a) is set at 0 Pa gauge. The hub and casing walls are specified with

the standard no-slip condition. The fluid medium in the baseline model is incompressible air at 15°C ( $\rho = 1.225 \text{ kg/m}^3$ ,  $\mu = 1.7894e-5 \text{ kg/(ms)}$ ).

With an approximate Reynolds number of  $2.8e5$ , the flow in the baseline duct is turbulent. Perhaps the most controversial step in the fluid flow modeling process is selection of an appropriate turbulence model to capture this flow characteristic. In this context, Britchford et al. [2] compared the  $k - \epsilon$  turbulence model and the Reynolds stress model, and reported that the mean velocity profile and shear stress are predicted better by the latter. Milanovic et al. [34] carried out RANS simulations for detailed sensitivity analysis of strutted compressor ducts, with the  $k - \omega$  and Spalart-Almaras turbulence models. Their computational predictions indicated good agreement with experimental data. Bhat and Sullerey [35] compared six different turbulence models for S-duct diffusers with flow control, and concluded that the  $k - \omega$  SST model could best reproduce their experimental data. On the other hand, Immonen [5] successfully used the  $k - \omega$  SST model in the constrained optimization of airfoil shapes. Based on these findings, the  $k - \omega$  SST model is chosen as the turbulence model for the present application. In the absence of measured values for the model constants at the inlet and outlet, here we rely on the default parameter values in ANSYS Fluent R16.0.

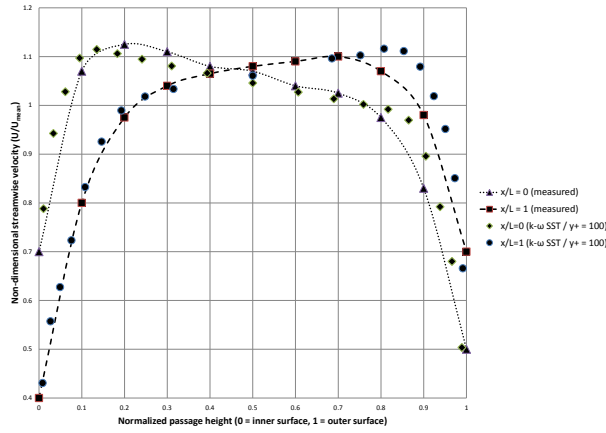
### 3.3. Model validation

#### 3.3.1. Simulation

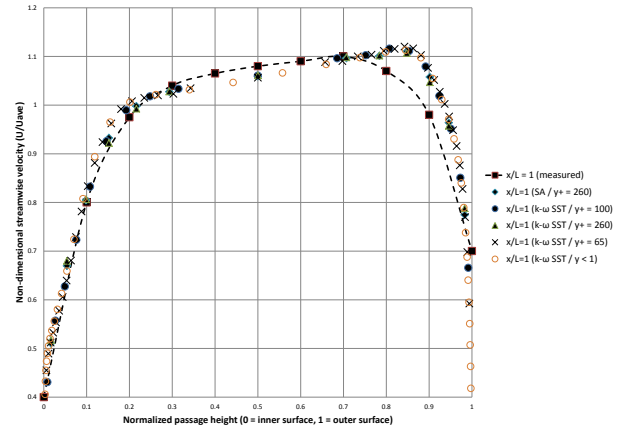
For the baseline CFD model, 1000 steady state iterations were carried out to ensure full flow field convergence, with final error residual values (continuity, velocity, turbulence) below  $10^{-8}$ . On a 2.6 GHz laptop computer, this took approximately 5 minutes (single core).

#### 3.3.2. Comparison to measurements

Figure 4a displays a comparison of the velocity magnitude profiles in the radial direction at  $x/L = 0$  (S-section entry) and  $x/L = 1$  (S-section exit) to the measured values presented by Britchford et al. [2, 29]. The results show a good agreement between the simulated and measured flow velocities, except near the casing wall at  $x/L = 1$  where the CFD simulation over-predicts velocity magnitudes. A similar local discrepancy at the S-duct exit was also



(a) Comparison to measurements.



(b) Sensitivity to model changes

Figure 4: Baseline model validation: Comparison of simulated velocity profiles at S-section entry ( $x/L = 0$ ) and exit ( $x/L = 1$ ) to measured values [2, 29]. The measured velocity profiles are connected with lines.

observed by Milanovic et al. [34], albeit on a strutted version of the baseline model; they attributed it to the shortcomings of the turbulence models. Note that, in the absence of error statistics for the measurements [2, 29], the significance of this local discrepancy between the simulated values and the reported measurements cannot be quantified.

Figure 9 displays a comparison of the normalized static pressure  $p_n = \frac{p-p_0}{P_0-p_0}$  profiles at  $x/L = 1$  relative to the measurements; the normalized static pressure underprediction in the vicinity of  $x/L = 1$  is consistent with Figure 4b. Elsewhere there is a good agreement with the measured values [29].

### 3.3.3. Sensitivity to mesh resolution and turbulence model

The specified mesh structure and inlet velocity yield a  $y+ \approx 100$  across the domain. Figure 4b displays the velocity magnitude at the S-duct exit  $x/L = 1$  for 4 different  $y+$  values ( $y+ \approx 260$  with 5365 cells at growth rate 1.3,  $y+ \approx 65$  with 18540 cells at growth rate 1.3,  $y+ < 1$  with 32136 cells at growth rate 1.3) for the  $k - \omega$  SST turbulence model. The highest resolution mesh among these is comparable to that used by Donghai et al. [26]. The figure also presents a comparison of the simulated velocity magnitudes between the  $k - \omega$  SST and the Spalart-Almaras (SA) turbulence models with  $y+ \approx 260$ . It is clear that



the baseline model flow simulation results, in particular the velocity discrepancy near the casing wall at  $x/L = 1$ , are not significantly affected by refinement of the boundary layer resolution or by the use of an alternative turbulence specification.

While academic literature often indicates  $y+ < 1$  as a requirement for the computational mesh (see e.g. [36]) for CFD simulation result accuracy, we have observed in practice that such high resolution is not necessary for accurate reproduction of general flow patterns. Based on our experience, the most important feature of a good (structured) computational mesh is low aspect ratio: Abrupt jumps in the adjacent cell dimensions distort the flow the most. Indeed, ANSYS Fluent is described to employ a  $y+$  independent wall formulation in all  $\omega$ -based turbulence models, thus making the overall resolution of the boundary layer more critical for accurate resolution of the flow than the actual numerical value of the  $y+$  [5, 33]. This implies that, in practical CFD-based shape optimization, meaningful and accurate comparisons between the performance of competing geometry alternatives can be carried out at much higher  $y+$  values than 1, provided that the computational meshes across the geometry alternatives are kept as identical as possible *and* the simulation parameters (e.g. iteration count) across the simulation cases are kept constant. This approach is utilized in the present work.

## 4. Shape optimization

### 4.1. Single-objective optimization

In this subsection, we consider optimization of the baseline annular S-duct shape with respect to the five objectives, defined in Equations (1), (3), (4), (5) and (6), separately.

#### 4.1.1. Model goodness-of-fit and prediction by RSM optimization

In this study, RSM identification is based on a DOE set of  $N = 500$  deformed shape candidates, each calculated with boundary conditions, mesh structure and iteration count as in the baseline model. None of the deformed cases displayed final residual values (continuity, velocity, turbulence) above  $10^{-8}$ , which indicates a good convergence of the flow field solutions.

Table 1 displays the goodness-of-fit statistics for all 25 response surface models, as identified by the row (model specification) and column (design objective) headers. In Table 1, each cell displays the leave-one-out cross-validation fit statistics  $R^2$ , MAE and MAESTD, separated by slashes. Clearly, RSM fitness improves as model complexity — the polynomial degree — is increased. This is an expected result, but it does not yet imply that a higher-order RSM should be preferred in shape optimization due to risk of over-fitting.

	CP	Urel	Urad	SP	TP
<b>RSM degree 1</b>	0.566 / 0.151 / 0.112	0.809 / 0.056 / 0.042	0.89 / 0.067 / 0.055	0.806 / 0.124 / 0.1	0.785 / 0.107 / 0.083
<b>RSM degree 2</b>	0.927 / 0.062 / 0.047	0.978 / 0.017 / 0.015	0.991 / 0.019 / 0.016	0.994 / 0.019 / 0.019	0.979 / 0.033 / 0.028
<b>RSM degree 3</b>	0.968 / 0.041 / 0.032	0.993 / 0.01 / 0.008	0.997 / 0.011 / 0.009	1 / 0.005 / 0.005	0.997 / 0.013 / 0.012
<b>RSM degree 4</b>	0.977 / 0.034 / 0.027	0.998 / 0.005 / 0.005	0.999 / 0.007 / 0.007	1 / 0.003 / 0.003	0.999 / 0.006 / 0.006
<b>RSM degree 5</b>	0.984 / 0.027 / 0.025	0.998 / 0.004 / 0.004	0.999 / 0.006 / 0.005	1 / 0.003 / 0.002	1 / 0.004 / 0.004

Table 1: RSM fit statistics.

The RSM polynomials referenced in the cells of Table 1 then yield optimal S-section shapes with respect to the objectives listed in the respective column headers, via constrained nonlinear optimization. Table 2 displays the predicted performance of the optimal annular S-ducts, and the corresponding performance metric evaluated from the baseline model. In Table 2, a cell  $(i, j)$  displays the predicted optimal value from the RSM model of degree  $i$  relative to metric  $j$ , which is also the optimization criterion for the cell's RSM. These results suggest that there may be room for improvement in the baseline model with respect to each of the design objectives, but this assertion must still be validated by CFD simulations.

	CP	Urel	Urad	SP	TP
<b>RSM degree 1</b>	0.380	0.136	0.199	6.51	0.0048
<b>RSM degree 2</b>	0.602	0.176	0.204	40.82	0.0214
<b>RSM degree 3</b>	0.645	0.167	0.231	42.81	0.0186
<b>RSM degree 4</b>	0.627	0.167	0.198	42.74	0.0210
<b>RSM degree 5</b>	0.622	0.170	0.222	42.61	0.0211
<b>Baseline model</b>	0.691	0.214	0.766	56.02	0.0288

Table 2: The predicted values from the optimal RSM models and the corresponding simulated values from the baseline model.

#### 4.1.2. Validation of optimal solutions by CFD

Table 3 and Table 4 summarize the results of CFD validation of the RSM predictions of Table 2. Note that Table 3 also shows an evaluation of the performance of each optimal S-duct profile relative to the four *other* design variables. For example, the last 7 rows of Table 3 display the simulated energy loss ( $TP$ ) values for *each* optimized RSM; yet only those in the last column are optimized with respect to minimum  $TP$ . The best-performing geometry model with respect to  $TP$  is the 4<sup>th</sup> degree polynomial RSM, identified and minimized with respect to  $TP$ , yielding an improvement of 26% (the underlined cell,  $TP = 0.0213$ ) relative to the baseline model ( $TP = 0.0288$ ).

Table 4 displays the relative prediction errors of the optimized RSM models. The errors are calculated by comparing the predicted values in Table 2 to the corresponding entries in Table 3. For example, the predicted  $TP$  value from 4<sup>th</sup> degree RSM degree ( $TP = 0.0210$ ) is compared to the corresponding CFD simulation result ( $TP = 0.0213$ ), yielding an error of 1.4%.

It is clear from Table 3 that, for each objective, the best performance is obtained from optimization with respect to that objective — a necessary condition for the credibility of the proposed approach and an indication that the proposed RSM models are indeed able to capture various dimensions of the design problem. Moreover, based on Table 3 and Table 4, the use of high order polynomial response surfaces is warranted for the present application: Linear models generally produce poor prediction quality, and, with only few exceptions, the prediction errors for polynomial models of degrees above 2 are smaller than those of widely used quadratic polynomial models. For each design objective, the best-performing shape is obtained from optimization by using 4<sup>th</sup> or 5<sup>th</sup> order polynomial RSMs.

#### 4.1.3. Properties of the optimal shapes

The optimal shapes obtained from single-objective optimization are displayed in Figure 5, which includes the best-performing (underlined) endwall profiles from Table 3. Note that the hub wall profiles for  $U_{rel}$  and  $U_{rad}$  are indistinguishable. Also note that the 4% zero deformation condition, originally imposed near the end points  $x/L = 0$  and  $x/L = 1$  of the

	CP	Urel	Urad	SP	TP	Variable
RSM degree 1	0.821	0.821	1.410	0.821	0.906	CP
RSM degree 2	0.632	0.857	1.281	0.689	0.770	CP
RSM degree 3	0.682	0.759	1.125	0.688	0.847	CP
RSM degree 4	0.603	0.823	1.280	0.690	0.821	CP
RSM degree 5	<u>0.595</u>	0.793	1.376	0.666	0.765	CP
Baseline case Cp	0.691					
Improvement	14%					
RSM degree 1	0.179	0.179	0.192	0.179	0.222	Urel
RSM degree 2	0.199	0.176	0.193	0.201	0.197	Urel
RSM degree 3	0.237	0.176	0.200	0.211	0.195	Urel
RSM degree 4	0.200	<u>0.172</u>	0.193	0.211	0.191	Urel
RSM degree 5	0.200	0.173	0.192	0.208	0.182	Urel
Baseline case Urel	0.214					
Improvement	20%					
RSM degree 1	0.813	0.813	0.228	0.813	1.165	Urad
RSM degree 2	0.884	0.545	0.221	0.966	0.986	Urad
RSM degree 3	1.124	0.643	0.232	1.027	0.994	Urad
RSM degree 4	0.841	0.532	0.221	1.030	0.955	Urad
RSM degree 5	0.823	0.637	<u>0.219</u>	0.992	0.850	Urad
Baseline case Urad	0.766					
Improvement	71%					
RSM degree 1	55.05	55.05	67.02	55.05	50.27	SP
RSM degree 2	43.74	48.06	64.54	43.73	46.07	SP
RSM degree 3	46.10	50.58	64.15	42.76	50.50	SP
RSM degree 4	44.82	51.76	64.53	42.76	48.77	SP
RSM degree 5	45.29	51.17	66.27	<u>42.70</u>	51.00	SP
Baseline case SP	56.02					
Improvement	24%					
RSM degree 1	0.0236	0.0236	0.0286	0.0236	0.0235	TP
RSM degree 2	0.0236	0.0244	0.0282	0.0228	0.0219	TP
RSM degree 3	0.0257	0.0227	0.0301	0.0231	0.0219	TP
RSM degree 4	0.0242	0.0242	0.0282	0.0231	<u>0.0213</u>	TP
RSM degree 5	0.0244	0.0226	0.0283	0.0231	0.0214	TP
Baseline case TP	0.0288					
Improvement	26%					

Table 3: CFD validation results of single-objective optimization for five distinct objective functions (last column) and different polynomial response surface model degrees. Each underlined cell value indicates the best validated optimization result relative to the chosen criterion; the improvement (%) it yields is reported relative to the baseline case.

	CP	Urel	Urad	SP	TP
RSM degree 1	116.2%	31.3%	14.1%	745.4%	389.6%
RSM degree 2	5.0%	0.2%	8.6%	7.1%	2.3%
RSM degree 3	5.7%	5.6%	0.5%	0.1%	17.7%
RSM degree 4	3.8%	3.0%	11.3%	0.1%	1.4%
RSM degree 5	4.3%	1.7%	1.4%	0.2%	1.4%

Table 4: Optimal polynomial RSM model prediction errors relative to CFD simulations.

S-section for shape smoothness, actually creates an artificial bend at  $x = 0.525$  m in some casing wall profiles, and thus may adversely affect the performance of these profiles.

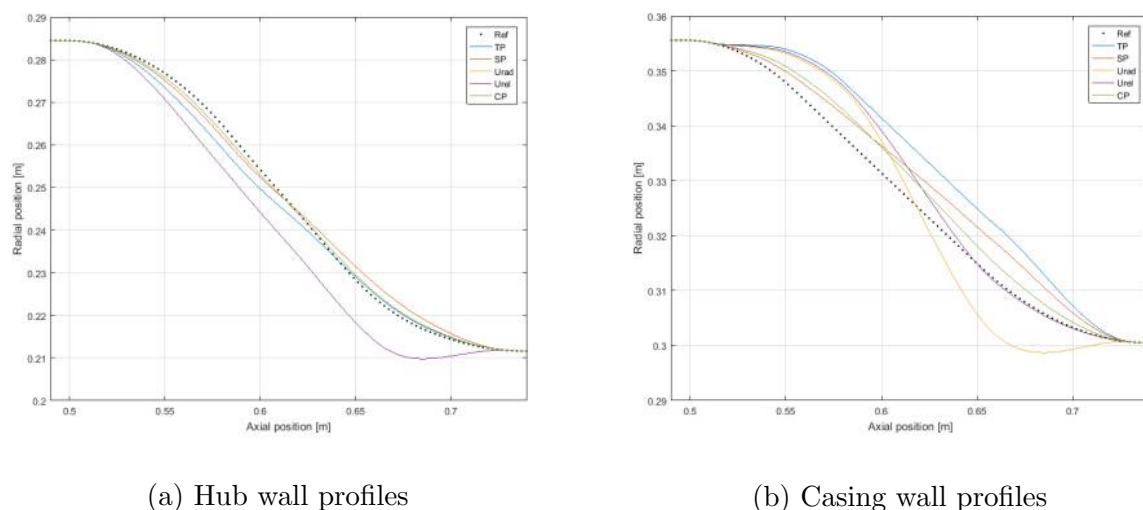


Figure 5: Single-objective optimization results: Optimal wall profiles vs. baseline model (dots). The hub wall profiles corresponding to optimal  $U_{rel}$  and  $U_{rad}$  performance are indistinguishable.

Figure 6 shows the  $C_p$  distribution of the  $CP$ -optimal geometry model from Table 3 relative to the baseline model. In the optimized duct, the  $C_p$  profile is more moderate on the inner wall, which helps reduce flow separation in that region [21].

Figure 7 presents a comparison of the static pressure in the flow field in the S-duct region. Clearly, the geometry model optimized relative to  $SP$  displays a more uniform static pressure field, with slightly damped streamwise gradients. Analogous to [21], such  $SP$ -optimal design also improves the energy efficiency ( $TP$ ) relative to the baseline model by 20%.

#### 4.1.4. Interdependence of the design objectives

A major goal of this article is to study the dependence between different shape optimization objectives for annular S-ducts. In the present subsection, we do this by a statistical correlation analysis. This is important not only for understanding the tradeoffs that one may have to make in the shape design process, but also because the RSM identification may yield better results with respect to some objectives than others. In the latter case, optimization could be carried out with respect to the most robust objective among the similar ones.

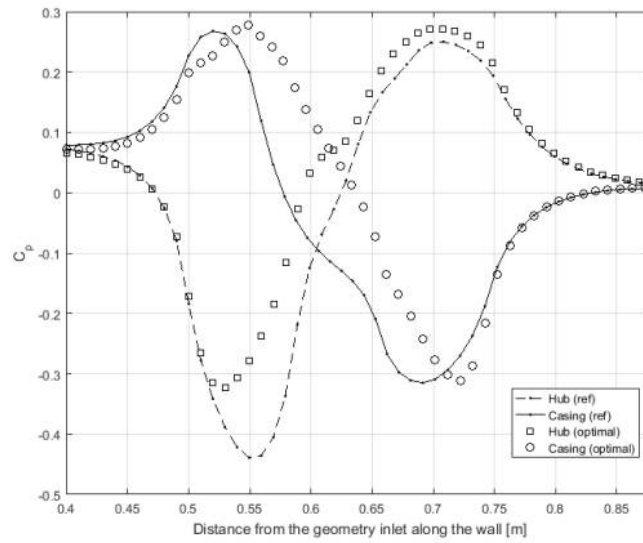
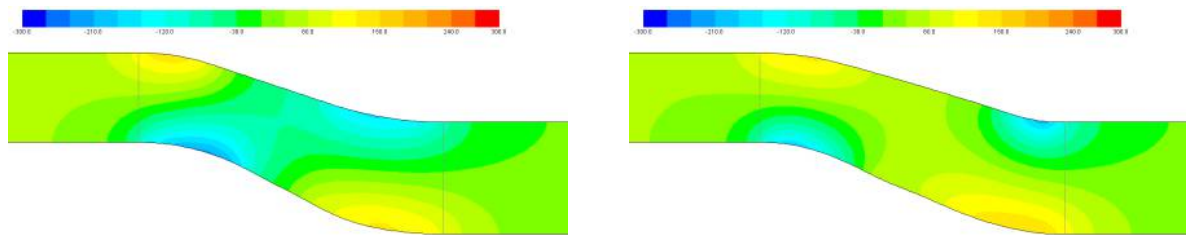


Figure 6: Comparison of  $C_p$  values on the hub and casing walls: 5<sup>th</sup> degree polynomial RSM optimization vs. baseline model reference.



(a) Baseline model.

(b) Optimal model (5<sup>th</sup> degree RSM).

Figure 7: Comparison of static pressure profiles: Baseline vs.  $SP$ -optimal

As we do not aim to assess the statistical dependence between the objective variables *in general*, but their dependence among the “*well-performing*” shape candidates, the data set of 500 shape candidates (samples) has to be processed before calculating correlations. For each of the 5 objectives, we only consider those samples with a better-than-median performance with respect to that objective; The correlation results and the corresponding statistical significance ( $p$ -values) are displayed in Table 5. For example, the last column ( $TP$ -opt) displays the variable correlations to  $TP$  among those samples for which the total pressure loss in the duct is less than the median total pressure loss value among all samples.

The  $p$ -values are reported in parentheses.

Not surprisingly, a relatively high correlation coefficient (0.81) is specifically observed between  $TP$  and  $SP$  in this sample subset, indicating that a low total pressure loss is closely related to low standard deviation of static pressure in the duct. However, perhaps more surprisingly, low energy losses do not seem to as be closely associated with uniform flow at the S-section exit. Indeed, optimizing the S-duct profile with respect to low radial flow does not seem to improve energy loss characteristics of the duct. And, conversely, the minimization of total pressure loss in fact appears to *increase* radial flow: The correlation coefficient  $-0.14$ , is statistically significant ( $p = 0.027$ ). To the author's knowledge, this phenomenon has not been reported in the literature before.

	CP-opt	Urel-opt	Urad-opt	SP-opt	TP-opt
<b>CP</b>	x	0.2 (0.0018)	-0.26 (2.9e-05)	0.72 (1.8e-39)	0.45 (1e-13)
<b>Urel</b>	0.16 (0.011)	x	0.18 (0.0045)	0.47 (6.4e-15)	0.59 (6.2e-25)
<b>Urad</b>	-0.21 (0.0007)	0.3 (1.3e-06)	x	-0.28 (1.1e-05)	-0.14 (0.027)
<b>SP</b>	0.59 (1.7e-24)	0.53 (1.3e-19)	-0.047 (0.46)	x	0.81 (3.2e-59)
<b>TP</b>	0.42 (5.9e-12)	0.64 (1.3e-30)	0.038 (0.55)	0.81 (1.8e-56)	x

Table 5: Correlations calculated among the best-performing samples. The  $p$ -values for testing the hypothesis that there is no relationship between the observed phenomena (null hypothesis) are displayed in parentheses. Note that the table is not symmetric, as the set of best-performing samples depends on the objective.

#### 4.1.5. Analysis of flow patterns

We conclude this section by investigating the flow patterns explaining Table 5. Based on Figure 5, for energy loss (objectives  $TP$ ,  $SP$ ,  $CP$ ) minimization relative to the baseline model, the casing profile is designed for increased streamwise area distribution in the S-section. Moreover, the hub profile is designed for increased convexity at the S-section inlet and for decreased concavity at the S-section outlet. These general features of the minimum-loss shapes are identical to those reported by Donghai et al. [26] who attribute the improved performance to a lower streamwise pressure gradient, which suppresses flow separation (Figure 8a).

On the other hand, again based on Figure 5, for flow uniformity (objectives  $U_{rel}$ ,  $U_{rad}$ ) relative to the baseline model, the hub profile is designed for increased convexity at the

S-section inlet and for increased concavity at the S-section outlet, with the minimum wall radius in the last bend extending lower than the model's minimum outlet radius. This arrangement results in a slightly separated flow on the hub, with reattachment taking place close to the S-section exit  $x/L = 1$ , and a flow turned nearly axial by the bend (Figure 8b). By reattachment, the boundary layer on the hub at  $x/L = 1$  is thin, and the flow velocity magnitude is thus close to uniform. As for casing, the profile is designed for increased concavity at the S-section inlet and for increased convexity at the S-section exit, with the minimum wall radius in the last bend extending lower than the model's maximum outlet radius. The Coandă effect at the bend turns the flow to almost fully axial near the casing before the S-section exit at  $x/L = 1$  (Figure 8b).

It should be pointed out that an ideal S-section outlet, displaying a purely axial flow, has no radial pressure gradient across the exit. As seen in Figure 9, at  $x/L = 1$ , the normalized static pressure  $p_n = \frac{p-p_0}{P_0-p_0}$  of the minimum  $U_{rad}$  model is uniformly close to zero, while that of the minimum  $TP$  model displays more a pronounced radial pressure gradient than the baseline model. This highlights the observation that energy loss minimization may in fact be detrimental for outflow uniformity in the present application.

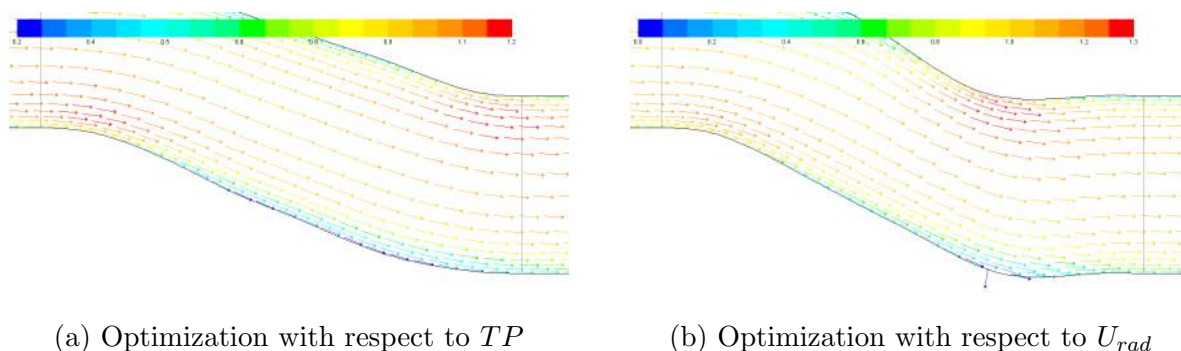


Figure 8: Flow patterns near the S-section exit  $x/L = 1$ .

#### 4.2. Multi-objective optimization

As energy loss minimization and outlet flow uniformity maximization turn out to be competing design objectives, it is interesting to study the extent to which they can be



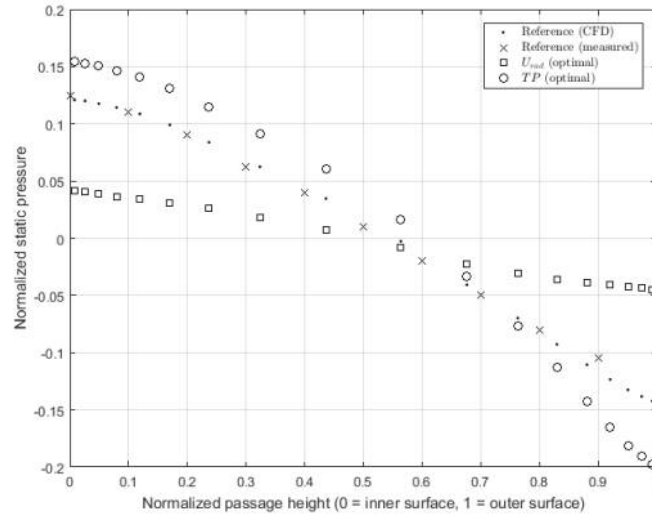


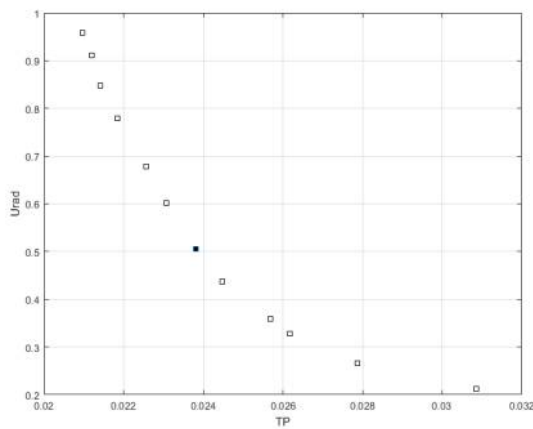
Figure 9: Comparison of normalized static pressure values  $p_n = \frac{p-p_0}{P_0-p_0}$  at the S-section exit  $x/L = 1$ .

optimized *simultaneously*. To this end, we can apply multi-objective optimization by using the best-fit models for  $TP$  (degree 4) and  $U_{rad}$  (degree 5) based on Table 3.

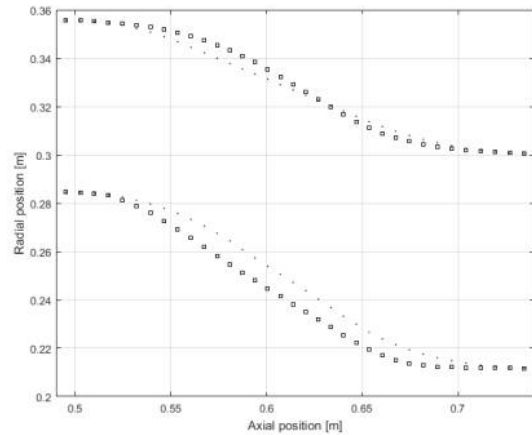
The Pareto optimal set of solutions, for which neither design objective can be improved without making the other worse, is displayed in Figure 10a. One of these Pareto optimum profiles is highlighted in Figure 10a, and it is compared to the baseline shape in Figure 10b. It yields a total pressure loss  $TP = 0.0243$ , at 2.0% RSM-to-CFD prediction error (15.6% improvement relative to the baseline model), and a normalized absolute radial velocity  $U_{rad} = 0.504$  at the S-duct exit, at 0.2% RSM-to-CFD prediction error (34.2% improvement relative to the baseline model). The corresponding S-section outflow behavior is displayed in Figure 11. Clearly, the optimal shape presented in Figure 10b displays a compromise between the features of minimum-loss shapes and those of maximally uniform outflow shapes, as listed in Subsection 4.1.4 and Subsection 4.1.5.

## 5. Discussion and conclusions

By applying the control node approach [5] and high order polynomial response surfaces, in this article we have proposed a computational approach for parametric shape optimization of annular S-ducts for attaining a minimum energy loss and a maximally uniform outlet flow.



(a) Pareto optimal set



(b) Optimal (squares) vs baseline model (dots)

Figure 10: Multi-objective optimization: The optimal endwall profile represents the filled square on the Pareto set.

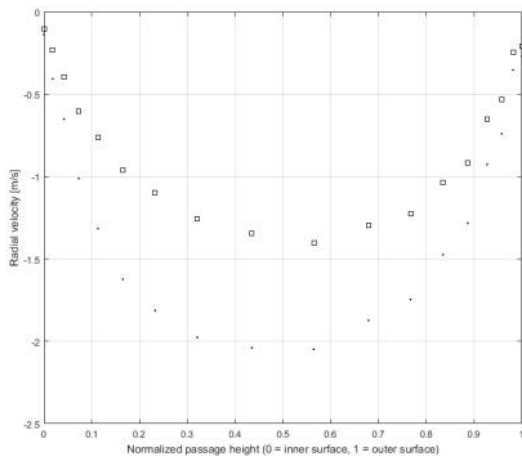
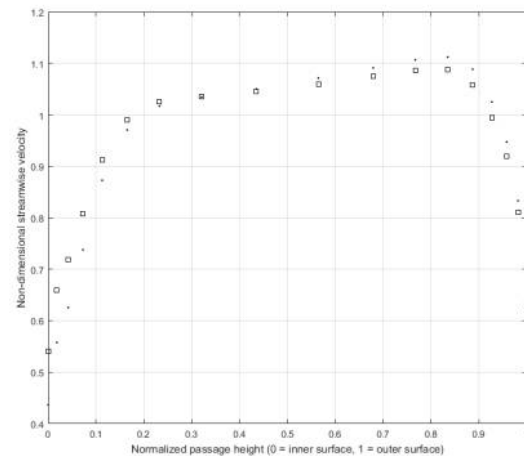
(a) Radial velocity at exit  $x/L = 1$ (b) Normalized velocity at exit  $x/L = 1$ 

Figure 11: Multiobjective optimization results: Optimal wall profiles (squares) vs. baseline model (dots).

The proposed low-parameter RSM models have been shown to display a good control of S-duct shapes with respect to 5 distinct numerical design objectives, and the merit of high order polynomial models has been demonstrated by accurate CFD-validated optimization performance across them. Indeed, for each of the five design objectives considered herein,

the best results were obtained by optimization on polynomial response surfaces of orders 4 or 5. Among others, this observation contrasts the findings of Immonen [5] who did not find merit in using polynomial response surface models of degrees higher than 2 for airfoil shape optimization with respect to drag and lift.

The “offline” optimization framework considered herein is based on a large set of input-output data — from CFD simulation cases on deformed shapes — that not only yields the RSM models, but can also be used to study the correlations between the design criteria. Based on such statistical analysis, we have concluded that, somewhat unexpectedly, the goals of minimizing the total pressure loss and achieving a uniform flow at the S-section outlet are contradictory. Indeed, shape optimization for maximum flow uniformity was shown to result in significantly different duct shapes than those obtained from shape optimization for minimum total energy loss. A multiobjective optimization on the RSM was nonetheless successfully utilized to simultaneously reduce the total pressure loss by 15.6% and the normalized absolute radial velocity by 34.2%, relative to the baseline model [3, 2, 29]. Such performance improvement potential may be beneficial, for example, in gas turbine engine design. On the other hand, since numerical optimization on polynomial RSMs is computationally cheap and can be carried out without high-end CFD software, our approach suggests an architecture for a practical offline decision support system: The designer invokes (in almost real time) independent RSM models, each addressing a separate aspect of the design problem, for optimal shape suggestions. Implementation of such decision support systems might be beneficial in many engineering applications beyond optimal S-duct design.

Perhaps the main drawback of the proposed shape optimization approach is that it is inherently 2-dimensional. An obvious direction for future research work is thus its generalization for 3-dimensional geometries.

## Acknowledgement

The author thanks the anonymous referees for their constructive criticism and for suggesting several improvements to the original manuscript.

## References

- [1] D. W. Bailey, The aerodynamic performance of an annular s-shaped duct, Ph.D. thesis, Loughborough University (1997).
- [2] K. M. Britchford, A. P. Manners, J. J. McGuirk, S. J. Stevens, Measurement and prediction of flow in annular s-shaped ducts, *Experimental Thermal and Fluid Science* 9 (1994) 197–205.
- [3] D. W. Bailey, K. M. Britchford, J. F. Carrote, S. J. Stevens, Performance assessment of an annular s-shaped duct, *ASME. J. Turbomach.* 119 (1) (1997) 149–156.
- [4] C. O. Dueñas, R. Miller, H. Hodson, J. Longley, Effect of length on compressor inter-stage duct performance, in: *ASME Turbo Expo 2007: Power for Land, Sea, and Air*, American Society of Mechanical Engineers, 2007, pp. 319–329.
- [5] E. Immonen, 2d shape optimization under proximity constraints by cfd and response surface methodology, *Applied Mathematical Modelling* 41 (2017) 508–529.
- [6] C. C. D. Ronco, R. Ponza, E. Benini, Aerodynamic shape optimization of aircraft components using an advanced multi-objective evolutionary approach, *Computer Methods in Applied Mechanics and Engineering* 285 (2015) 255–290.
- [7] H. Kim, C. Yang, A new surface modification approach for cfd-based hull form optimization, *Journal of Hydrodynamics Ser. B* 22 (5) (2010) 520–525.
- [8] D. Vucina, I. Marinic-Kragic, Z. Milas, Numerical models for robust shape optimization of wind turbine blades, *Renewable Energy* 87 (2) (2016) 849–862.
- [9] S. M. A. N. R. Abadi, A. Ahmadpour, S. M. N. R. Abadi, J. P. Meyer, Cfd-based shape optimization of steam turbine blade cascade in transonic two phase flows, *Applied Thermal Engineering* 112 (2017) 1575 – 1589.
- [10] E. Papoutsis-Kiachagias, J. M. N. Magoulas, C. Othmer, K. Giannakoglou, Noise reduction in car aerodynamics using a surrogate objective function and the continuous adjoint method with wall functions, *Computers & Fluids* 122 (2015) 223–232.
- [11] M. Palacz, J. Smolka, W. Kus, A. Fic, Z. Bulinski, A. J. Nowak, K. Banasiak, A. Hafner, Cfd-based shape optimisation of a co<sub>2</sub> two-phase ejector mixing section, *Applied Thermal Engineering* 95 (2016) 62–69.
- [12] W. Yang, J. A. Feinstein, A. L. Marsden, Constrained optimization of an idealized y-shaped baffle for the fontan surgery at rest and exercise, *Computer Methods in Applied Mechanics and Engineering* 199 (3336) (2010) 2135 – 2149.
- [13] S. M. J. M. Akherat, K. Cassel, M. Boghosian, M. Hammes, F. Coe, A predictive framework to elucidate venous stenosis: Cfd & shape optimization, *Computer Methods in Applied Mechanics and Engineering* 321 (2017) 46 – 69.

- [14] R. H. Myers, D. C. Montgomery, C. M. Anderson-Cook, *Response Surface Methodology: Process and Product Optimization Using Designed Experiments*, John Wiley & Sons, 2009.
- [15] J. I. Madsen, W. Shyy, R. T. Haftka, Response surface techniques for diffuser shape optimization, *AIAA Journal* 38 (9) (2000) 1512–1518.
- [16] H. Sun, S. Lee, Response surface approach to aerodynamic optimization design of helicopter rotor blade, *International Journal for Numerical Methods in Engineering* 64 (1) (2005) 125–142.
- [17] S. A. I. Bellary, A. Husain, A. Samad, Effectiveness of meta-models for multi-objective optimization of centrifugal impeller, *Journal of Mechanical Science and Technology* 28 (12) (2014) 4947–4957.
- [18] M. B. Giles, N. A. Pierce, An introduction to the adjoint approach to design, *Flow, Turbulence and Combustion* 65 (3) (2000) 393–415.
- [19] T. Ghisu, M. Molinari, G. Parks, W. Dawes, J. Jarrett, P. Clarkson, Axial compressor intermediate duct design and optimisation, in: 48th AIAA/ASME/ASCE/AHS/ASC Structures, Structural Dynamics, and Materials Conference, 2007, p. 1868.
- [20] F. Wallin, L.-E. Eriksson, Response surface-based transition duct shape optimization, in: *ASME Turbo Expo 2006: Power for Land, Sea, and Air*, 2006, pp. 1465–1474.
- [21] H. Lu, X. Zheng, Q. Li, A combinatorial optimization design method applied to s-shaped compressor transition duct design, *Proceedings of the Institution of Mechanical Engineers, Part G: Journal of Aerospace Engineering* 228 (10) (2014) 1749–1758.
- [22] E. M. Naylor, C. O. Dueñas, R. J. Miller, H. P. Hodson, Optimization of nonaxisymmetric endwalls in compressor s-shaped ducts, *Journal of Turbomachinery* 132 (1) (2010) 011011.
- [23] I. Yurko, G. Bondarenko, A new approach to designing the s-shaped annular duct for industrial centrifugal compressor, *International Journal of Rotating Machinery*.
- [24] M. K. Gopaliya, M. Kumar, S. Kumar, S. M. Gopaliya, Analysis of performance characteristics of s-shaped diffuser with offset, *Aerospace Science and Technology* 11 (2) (2007) 130 – 135.
- [25] A. Stronach, A. Birk, Experimental and computational investigation of losses in a circular to oblong diffusing gas turbine transition duct with offset, in: *ASME Turbo Expo 2000: Power for Land, Sea, and Air*, 2000.
- [26] D. Jin, X. Liu, W. Zhao, X. Gui, Optimization of endwall contouring in axial compressor s-shaped ducts, *Chinese Journal of Aeronautics* 28 (4) (2015) 1076–1086.
- [27] R. B. M.D. McKay, W. Conover, A comparison of three methods for selecting values of input variables from a computer code, *Technometrics* 21 (2) (1979) 239–245.
- [28] M. G. Rose, Non-axisymmetric endwall profiling in the hp ngvs of an axial flow gas turbine, in: *ASME 1994 International Gas Turbine and Aeroengine Congress and Exposition*, 1994.
- [29] K. M. Britchford, The aerodynamic behaviour of an annular s-shaped duct, Ph.D. thesis, Loughborough

University (1998).

- [30] H. G. Bae, S. H. Park, J. H. Kwon, Ego method for diffusing s-duct shape design, in: International Conference on Computation Fluid Dynamics, Vol. 7, 2012.
- [31] M. K. Gopaliya, P. Goel, S. Prashar, A. Dutt, Cfd analysis of performance characteristics of s-shaped diffusers with combined horizontal and vertical offsets, *Computers & fluids* 40 (1) (2011) 280–290.
- [32] K. Deb, *Multi-Objective Optimization Using Evolutionary Algorithms*, John Wiley & Sons, 2001.
- [33] ANSYS, Inc., *ANSYS Fluent R15 User's Guide* (2013).
- [34] I. M. Milanovic, J. Whiton, R. V. Florea, S. Lynch, G. Tillman, L. W. Hardin, M. Stucky, Rans simulations for sensitivity analysis of compressor transition duct, in: 50th AIAA/ASME/SAE/ASEE Joint Propulsion Conference, 2014, p. 3631.
- [35] S. Bhat, R. Sullerey, An assessment of turbulence models for s-duct diffusers with flow control, in: ASME 2013 Gas Turbine India Conference, American Society of Mechanical Engineers, 2013, pp. V001T01A005–V001T01A005.
- [36] L. R. C. T. M. Resource, 2dn00: 2d naca 0012 airfoil validation case, [http://turbmodels.larc.nasa.gov/naca0012\\_val.html](http://turbmodels.larc.nasa.gov/naca0012_val.html), [Online; accessed 9-July-2017] (2014).